First comparisons of local ion measurements in the inner magnetosphere with energetic neutral atom magnetospheric image inversions: Cluster-CIS and IMAGE-HENA observations

Claire Vallat,[1] Iannis Dandouras,[1] Pontus C:son Brandt,[2] R. DeMajistre,[2] Donald G. Mitchell,[2] Edmond C. Roelof,[2] Henri Rème,[1] Jean-André Sauvaud,[1] Lynn Kistler,[3] Christopher Mouikis,[3] Malcolm Dunlop,[4] and André Balogh[5]

Received 5 September 2003; revised 17 December 2003; accepted 24 February 2004; published 21 April 2004.

[1] Data provided by the CIS (Cluster Ion Spectrometry) instruments on board the Cluster spacecraft are used to survey recent crossings of the inner magnetosphere and ring current. CIS is capable of obtaining full three-dimensional ion distributions (about 0 to 40 keV/q) with one spacecraft spin time resolution and with mass-per-charge composition determination. Events are selected for which the Cluster spacecraft are within the field of view of the HENA (high-energy neutral atom) imager on board IMAGE. HENA provides energetic neutral atom images with a high geometric factor and with a 120° × 360° field of view over the spin. The H^+ ion distribution functions obtained in situ by CIS are then compared to the ones deduced by inverting the HENA hydrogen neutral atom images for the overlapping energy range of the two instruments (27–39 keV). This analysis concerns events obtained both during well-developed ring current conditions (e.g., 18 April 2002 event) and during quiet magnetospheric conditions (e.g., 9 August 2001 event). The results show the consistency between the ion fluxes deduced from energetic neutral atom (ENA) image inversions and the fluxes measured locally. They thus show the complementarity of the two approaches. The locally measured fluxes provide the "ground truth," and they give the detailed ion distributions. ENA images allow to situate local measurements into a global context and to position them with respect to the ring current large-scale structure. Our results also show the limitations of the ion fluxes deduced from the ENA image inversions for images taken from a single vantage point, with a substantial scatter of the inversion fluxes with respect to the in situ measured ones and a more limited dynamic range. *INDEX TERMS:* 2778 Magnetospheric Physics: Ring current; 2730 Magnetospheric Physics: Magnetosphere—inner; 2760 Magnetospheric Physics: Plasma convection; 2740 Magnetospheric Physics: Magnetospheric configuration and dynamics; *KEYWORDS:* inner magnetosphere, neutral atom image inversions, ring current

Citation: Vallat, C., et al. (2004), First comparisons of local ion measurements in the inner magnetosphere with energetic neutral atom magnetospheric image inversions: Cluster-CIS and IMAGE-HENA observations, *J. Geophys. Res.*, *109*, A04213, doi:10.1029/2003JA010224.

1. Introduction

[2] The existence of a ring current forming around the Earth was first suggested by *Singer* [1957], who showed that a westward electric current was produced by the gradient drift of energetic particles (~1 keV to a few hundred of keV) trapped in the geomagnetic field. The effects of this current can be represented to an equivalent current that is toroidal-shaped and flowing around the Earth at geocentric distances from about 2 R_E to 9 R_E.

[3] The real current system of the inner magnetosphere is of course of a more complex nature but can essentially be described as a current system driven by the ring current (and plasma sheet) pressure gradients. During geomagnetic storm main phases the ring current pressure is centered around midnight. The resulting pressure driven currents produce a net westward current flowing on the outer edge of the ring current. Off equator, the current connects to the ionosphere and constitutes a significant part of the region 2 current system. The ring current evolution is driven by particle injections during geomagnetic activity increase and by the loss mechanisms [*Daglis et al.*, 1999]. The main process of ring current decay is charge exchange between ring current ions with the cold (~1000 K) neutral atoms

[1]Centre d'Etude Spatiale des Rayonnements, Toulouse, France.
[2]Applied Physics Laboratory, Johns Hopkins University, Laurel, Maryland, USA.
[3]Space Science Center, University of New Hampshire, Durham, New Hampshire, USA.
[4]Rutherford Appleton Laboratory, Didcot, UK.
[5]Blackett Laboratory, Imperial College, London, UK.

0148-0227/04/2003JA010224$09.00

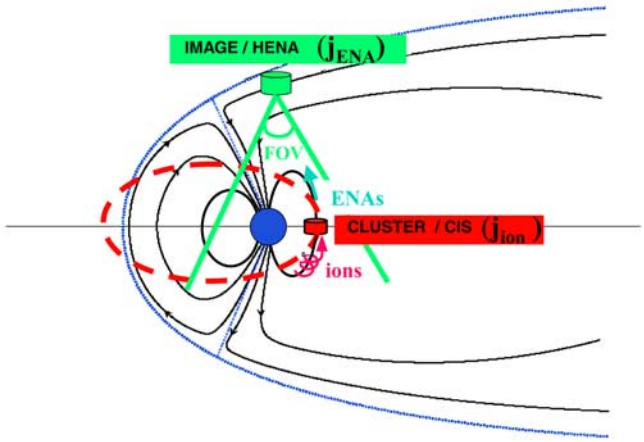

Figure 1. HENA (IMAGE) and CIS (Cluster) ionic flux correlation principle: events were chosen for which Cluster was at its perigee (equator pass), and situated within the HENA's field of view. ENAs fluxes recorded by HENA are used to trace back the ion population, mainly coming from the ring current region and measured in situ by CIS, which produced these ENAs through charge exchange.

forming the exosphere, mainly composed of hydrogen atoms [*Chamberlain*, 1963; *Rairden et al.*, 1986].

[4] Another important loss process, contributing to the ring current decay, is the coulomb collisions with the cold plasmaspheric ions, but this mechanism can be considered as negligible for ions with energies above 10 keV [*Jordanova et al.*, 1996]. Since this study is limited to ions with energies above 27 keV, this process will not be considered here. The wave/particle interactions play also an important role in the ring current decay at high energies (above a few tens of keV) [*Daglis et al.*, 1999] but do not need to be taken into account in this study (energies below 39 keV).

[5] The three main singly charged ion species interact with cold hydrogen atoms of the exosphere as follows:

$$H^+ + H_{cold} \text{ -> } H_{ENA} + H^+$$

$$O^+ + H_{cold} \text{ -> } O_{ENA} + H^+$$

$$He^+ + H_{cold} \text{ -> } He_{ENA} + H^+.$$

These interactions give rise to the production of energetic neutral atoms (ENAs). The energy of the incident ions is almost entirely transferred to the charge exchange produced ENAs, which then propagate along nearly rectilinear ballistic trajectories. The straight-line paths of the energetic neutral atoms suggest that they can be used to form an image of the ENA emitting regions, mostly corresponding to the ring current region [*Williams et al.*, 1992].

[6] The ENA images thus contain quantitative information of the magnetosphere-exosphere interaction processes on a global scale. The ENA flux, measured in each pixel of an image, is the line of sight integral (along the line of sight direction of the pixel) of the unidirectional ion fluxes multiplied by the local density of the neutral exospheric gas and by the charge exchange cross section between the two species (see also section 2.3, equation (2)) [*Roelof*, 1987]. This means that the extraction of quantitative information on the ion distributions from the image, which contains an admixture of information on energetic ions and cold neutral distributions, requires the inversion of the ENA image [*Roelof and Skinner*, 2000; *Perez et al.*, 2001].

[7] In this study we will compare the ionic fluxes measured directly inside the ring current region (by the Cluster Ion Spectrometer) to the ones deduced from ENA image inversions, using the constrained linear method [*DeMajistre et al.*, 2004] for a selected energy range (27 to 39 keV): from an ENA image (provided by the High Energy Neutral Atom imager on board IMAGE), the method traces back the ionic population. Events are selected for which one of the Cluster spacecraft is within a pixel of the inverted image while passing through the equator (see Figure 1). As we will see, the results confirm the charge exchange as being the main process of ring current's decay, but they also show the consistency and the limitations of the inversion method as an estimator of global ring current's shape and fluxes, for disturbed period events as well as for quiet ones.

2. Instrumentation and Method of Analysis

2.1. Cluster-CIS: Local Measurements

[8] The Cluster mission is based on four spacecraft launched on similar elliptical polar orbits with a perigee at about 4 R_E [*Escoubet et al.*, 2001]. This allows Cluster to cross the ring current region from south to north during every perigee pass and to obtain its latitudinal profile.

[9] The Cluster Ion Spectrometry (CIS) experiment on board Cluster consists of the two complementary spectrometers Hot Ion Analyzer (HIA) and Composition and Distribution Function Analyzer (CODIF) and provides the three-dimensional ion distributions with one spacecraft spin (4 s) time resolution [*Rème et al.*, 2001]. Furthermore, the mass-resolving spectrometer CODIF provides the ionic composition of the plasma for the major magnetospheric species (H^+, He^+, He^{++}, and O^+), from the thermal energy to about 40 keV/e, covering thus a large part of the ring current energy range [*Milillo et al.*, 2003]. The magnetic field data used come from the FGM (Fluxgate Magnetometer) experiment on board Cluster [*Balogh et al.*, 2001].

2.2. IMAGE-HENA: Global ENA Environment

[10] The IMAGE spacecraft was launched in March 2000 into an elliptical polar orbit with an apogee altitude of 7.2 R_E and a perigee altitude of 1000 km [*Burch*, 2000]. On board IMAGE, the HENA (high-energy neutral atoms) imager is used to determine the velocity, arrival direction and mass of ENAs in the 10–500 keV energy range. From these data it generates images of ENA source regions in the inner magnetosphere with a $\sim 6^\circ$ angular resolution [*Mitchell et al.*, 2000]. Because of the IMAGE orbit, HENA permits a global view of the ENA emission sources, such as the ring current population and the near-Earth plasma sheet, when the spacecraft is outside the radiation belts. Using the properties of the charge exchange process (ENAs keep almost the same energy and momentum as parent ions), ENAs are used like photons in order to form an image of the energetic ion distribution. A numerical method was thus developed, which through ENA image inversions gives the equatorial distribution function of the parent ions.

[11] This constrained linear inversion technique, used here, has been reported briefly by *C:son Brandt et al.* [2002a] and in more detail by *DeMajistre et al.* [2004]. Here we only outline the method.

2.3. Constrained Linear Method

[12] The count in each pixel of an ENA image, C_i, can be represented by the measurement equation:

$$c_i = \int_0^{\infty}\int_0^{\infty}\int_0^{2\pi}\int_0^{\pi} \sin\varepsilon A_i(\varepsilon,\beta,E,t) j_{ena} d\varepsilon d\beta dE dt, \qquad (1)$$

where A_i is the response of the pixel i to an ENA intensity j_{ena} at time t, energy E, and angular position ε and β. The ENA intensity from charge exchange can be written as

$$j_{ena} = \int_0^{Se} n^H(s)\sigma_H^{10}(E) j_{ion}(s,E) ds + j_{ena}^e(s_e), \qquad (2)$$

where s is the distance along the line of sight determined by ε and β, n^H is the number density of hydrogen, σ_H^{10} is the charge exchange cross section for protons on hydrogen, and j_{ion} is the ion flux. Below 3.5 R_E, the neutral hydrogen gas distribution n^H was fitted to the results by *Rairden et al.* [1986] using the following expression:

$$n^H(r,\varphi) = a\exp\left[be^{-cr} - \frac{r}{H(\varphi)}\right],$$

where

$$H(\varphi) = H_0(1 - k\cos\varphi)$$

with

$$\begin{aligned} a &= 3300\ \mathrm{cm}^{-3} \\ b &= 17.5 \\ c &= 1.5\ \mathrm{R_E}^{-1} \\ H_0 &= 1.46\ \mathrm{R_E} \\ k &= 0.3. \end{aligned}$$

Here, φ is the solar zenith angle from the Earth-Sun axis. For $r > 3.5$ R_E we used the model by *Østgaard et al.* [2003], which is based on Lyman-α measurements by the GEO detector on board IMAGE. Since only values from dusk to midnight were available for the Østgaard model, we extended the Østgaard model in the dayside with the dusk values. The Rairden and Østgaard models were matched to be continuous in the first derivative. For more details see *DeMajistre et al.* [2004].

[13] The second term j_{ena}^e is the contribution of ENA flux from the interaction between the ring current and the oxygen of the upper atmosphere at the exobase, which is treated as ENA emissions from a hard shell at 350 km altitude. The low-altitude interaction has been treated extensively by *Roelof* [1997]. The limit of integration, s_e, is either the point where the line of sight first intersects the exobase, or $+\infty$ for lines of sight with no such intersection. *DeMajistre et al.* [2004] showed that equation (1) can be approximated by numerical quadrature in the form of

$$c_i = \sum_p \sum_k \sum_l b_{ikl}^p\, j_{ion}^p(L_l, \phi_k), \qquad (3)$$

where the quadrature weights b_{ikl}^p are determined by computing an integral with a four-point integration scheme. The ion flux $j_{ion}^p(L_l, \phi_k)$ is expressed in L-shell and local time bins (L, φ) in the equatorial plane. Equation (3) is thus a well-defined, linearized forward model for ENA emissions. In the present formulation a dipole magnetic field is used. Furthermore, inversion results from a single vantage point cannot resolve pitch angle distributions (PAD), since only ENAs originating from a given pitch angle ions can reach the imager. We thus assume pitch angle isotropy. The linear equation system in equation (3) can be solved by a constrained linear inversion technique and can be written:

$$J_{ion} = \left(K^T\sigma_C^{-2}K + \gamma H\right)^{-1} K^T\sigma_C^{-2}C, \qquad (4)$$

which, for appropriate values of γ and H, has a unique solution. Solutions of this form have been treated extensively by other authors [see, e.g., *Twomey*, 1977; *Rodgers*, 2000; *Menke*, 1989].

[14] Not surprisingly, the inversion results are sensitive to both the constraint type and constraint strength. We have used two different constraint types in the inversion algorithm: the Markhov and the second derivative (D2) constraint. Both constraints are explained in more detail by *DeMajistre et al.* [2004]. Tests have shown that for our vantage point the Markhov constraint appear to be better at obtaining morphology correctly rather than absolute proton flux and the D2 constraint obtains better absolute proton fluxes. To combine the advantages of both constraints, we use the Markhov constraint to optimize the constraint strength of the D2 constraint, which is subsequently applied the real data. We describe the method of this optimization briefly: An approximate model of the source ion distribution is used to simulate an ENA image from the actual vantage point of the IMAGE spacecraft for the particular event in question. Noise is added to the ENA image and an initial gamma is used to invert the image using the Markhov constraint. The resulting ion distributions are then compared to the input model ion distribution; the gamma is changed and new inversion applied to the ENA image. The new result is again compared with the initial input model ion distribution. This is done until the difference between the retrieved ion distribution and the initial input model distribution is as small as possible. Note that up to this point no data has been introduced. The result of this exercise is a constraint strength optimized to obtain the inversion result which is closest to reality. One can then wonder if the gamma will be completely different for a different input model distribution. We have tested how the model distribution morphology (radial and local time position of the model distribution) affects the gamma and found that significant changes occur when the local time position changes 6 hours or more. Therefore we can for this first step eyeball the ENA images to determine the approximate local time position of the input model distribution.

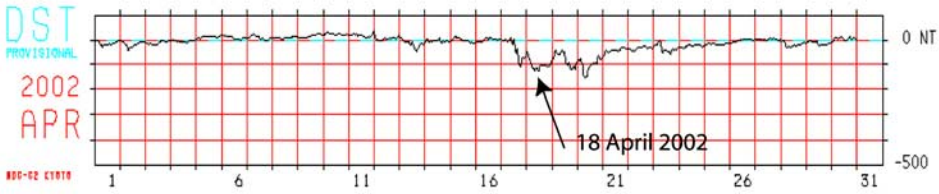

Figure 2. *Dst* index values for April 2002. On 18 April 2002, the main phase of a storm is observed, while Cluster is passing through perigee. At 0800 UT, *Dst* index was about −126.

[15] The resulting gamma will be applied to the Markhov constraint on the real data to obtain an ion distribution. However, we are not done yet, since we know that the Markhov constraint is suitable for achieving global morphology and not absolute values. We therefore take the retrieved ion distribution and simulate an ENA image. This ENA image is then inverted using the D2 constraint. The retrieved ion distribution is compared with the ion distribution retrieved using the Markhov constraint; the value of gamma is changed, until the differences (between the initial ion distribution, retrieved using the Markhov constraint, and the ion distribution retrieved using the D2 constraint) are small. We have, in fact, tried to guarantee that the resulting gamma is optimized such that the morphology is as close to reality as possible.

3. Observations and Analysis: 18 April 2002

3.1. Context

[16] During the 18 April 2002 event, the geomagnetic indices recorded a very disturbed period, with Kp = 6- and a *Dst* ∼ −126 nT. As can be seen in Figure 2, a storm-time ring current was at its main phase. At around 0812 UT, a substorm onset was observed by the Far Ultra Violet experiment on board IMAGE [*Mende et al.*, 2000]. Figure 3 shows a plot of the 75–105 keV proton fluxes measured by the Synchronous Orbit Particle Analyzer (SOPA) on board the Los Alamos National Laboratory (LANL) 1991-080 satellite during this substorm. We can see that a gradual decrease of the proton fluxes started around 0630 UT, which is consistent with a substorm growth phase in which the magnetic field stretches and the satellite drops out of the central plasma sheet. At about 0755 UT there is a sharp increase of proton fluxes followed by a larger and more gradual increase starting at around 0810 UT and peaking at around 0837 UT. The 1991-080 satellite was located between 1930 and 2133 MLT for the 0630–0837 UT interval. The GOES-10 magnetic field data showed a rapid (∼1 min) decrease in the x-component and increase of the z-component of the magnetic field at around 0810 UT, that are clear signatures of a substorm dipolarization. The GOES-10 satellite was around 2200 MLT for this measurement.

[17] For this period, the four Cluster spacecraft have a distance separation of about 100 km. SC 1 is crossing the equator first, followed by SC4, SC2, and SC3, respectively. SC 4 is crossing the equator at 0849 UT, in the evening sector (∼2100 MLT), during the main phase of the substorm. At 0900 UT, IMAGE was at its apogee (Ilat ∼ 81.8°, evening sector), allowing Cluster to be inside the HENA's field of view while passing through equator.

3.2. Observations

[18] Figures 4 and 5 present CODIF and FGM data from SC 4 for this event. From top to bottom, Figure 4 shows, for the proton population, the energy-time spectrograms in flux units (ions/cm^2 sr s keV), the pitch-angle distribution (in flux units) for two different energy ranges: 27 to 39 keV (which is the HENA/CIS overlap energy range) and 25 to 200 eV, the proton density, and the magnetic field components, in GSM coordinates. Figure 5 gives the same information but for the O^+ population. Cluster was in the southern lobe until 0724 UT, then it crossed a first boundary, situated at |Ilat| ∼ 70°, entering into the southern plasma sheet boundary layer. The region encountered (referenced as region PS on the spectrogram) corresponds to auroral field lines and is mainly characterized by an increase of the low-energy flux (below 200 eV) for protons as well as for oxygen ions, resulting in a jump on the ion density. At these energy ranges, hydrogen ions, as well as the oxygen ones, present a field-aligned (Southern Hemisphere) and anti-field-aligned (Northern Hemisphere) pitch angle distribution, which indicates the existence of upwelling protons and oxygen ions, escaping from the ionosphere [*Sauvaud et al.*, 2004]. Particles with energies above 1 keV present a much more isotropic distribution.

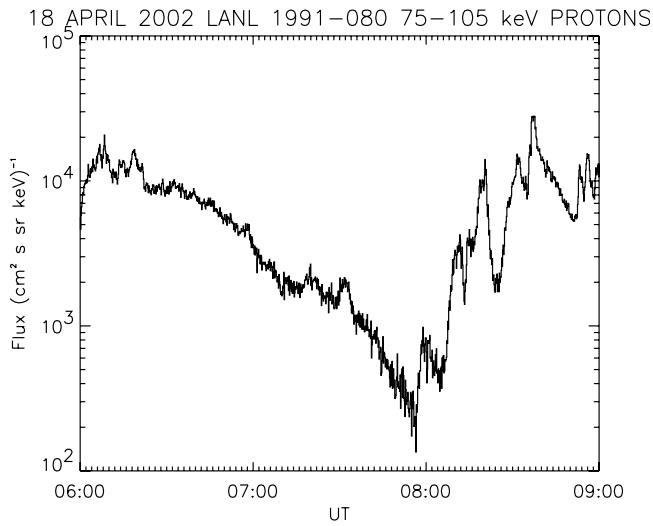

Figure 3. The 75–105 keV proton fluxes measured at the geostationary orbit by SOPA on board the LANL 1991-080 spacecraft, between 1900 and 2200 MLT.

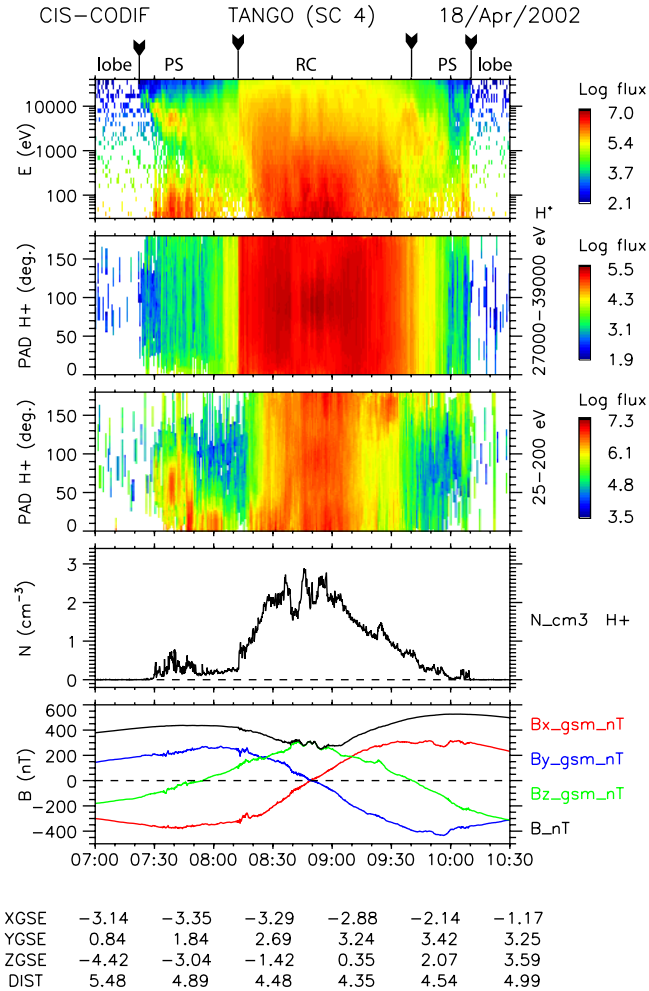

XGSE	−3.14	−3.35	−3.29	−2.88	−2.14	−1.17
YGSE	0.84	1.84	2.69	3.24	3.42	3.25
ZGSE	−4.42	−3.04	−1.42	0.35	2.07	3.59
DIST	5.48	4.89	4.48	4.35	4.54	4.99

Figure 4. Cluster spacecraft 4 ion and magnetic field data for 18 April 2002, between 0700 and 1030 UT. From top to bottom: hydrogen spectrogram in particle flux units (cm^{-2} sr^{-1} s^{-1} keV^{-1}), pitch-angle-time spectrograms for the HENA/CIS overlap energy range (27 to 39 keV) and for the low energies (25 to 200 eV), proton density, magnetic field components (GSM system), and the Cluster position in GSE coordinates (in R_E).

[19] At 0812 UT, SC 4 encounters a very sharp boundary, as seen in the proton and oxygen pitch angle distributions measured by CODIF and in the FGM data (region referenced as RC on the spectrogram): a sharp jump in the ionic flux (more than one order of magnitude) and density values (factor of ∼4), as well as the onset of disturbances in the magnetic field, are the main signatures of the transition. For 33 keV protons (representative of the 27–39 keV energy band), and for a 423 nT magnetic field, as measured when entering into the ring current particle population (0812 UT), the gyroradius is 62 km. The sharp boundary observed for these particles is within one three-dimensional distribution acquisition (8 s for this mode), i.e., within about 37 km along the spacecraft trajectory (Vsc = 4.6 km/s). It thus appears that the ring current boundary characteristic thickness is within one ion gyroradius. This boundary first appears at L ∼ 5 for the H^+ higher energy range spectrogram (above 2 keV), revealing an energy dispersion. At low energies, particles field-aligned and anti-field-aligned are now simultaneously observed in each hemisphere. At higher energies (27 to 39 keV), the major part of the proton population is trapped and centered at 90° pitch angle, showing that this population is the lower-energy part of the ring current. All these indicate the interface of the ring current region and of the plasma sheet, the spacecraft entering into the ring current at 0812 UT.

[20] Two different features appear then alternatively: a trapped H+ population (pitch angle ∼ 90°), with a density around 2.5 cm^{-3} (0.3 cm^{-3} for the 27–39 keV energy range), coinciding with a decrease of the magnetic field magnitude, is alternating on the CODIF spectrograms with a second population less dense (below 2.0 cm^{-3}, or 0.02 cm^{-3} for the 27–39 keV energy range), field-aligned and anti-field-aligned coinciding with an increase in the magnetic field magnitude. The numerous alternations between these two types of population characterized by a slight increase on the B magnitude as well as on the proton density reveal the presence of a boundary crossed a few times by Cluster. Note that the very close spacing of the Cluster spacecraft, for this event, does not allow using interspacecraft comparisons to further analyze this boundary motion. The simultaneous evolution on the proton density and magnetic field reveals anyway the presence of strong diamagnetic effects.

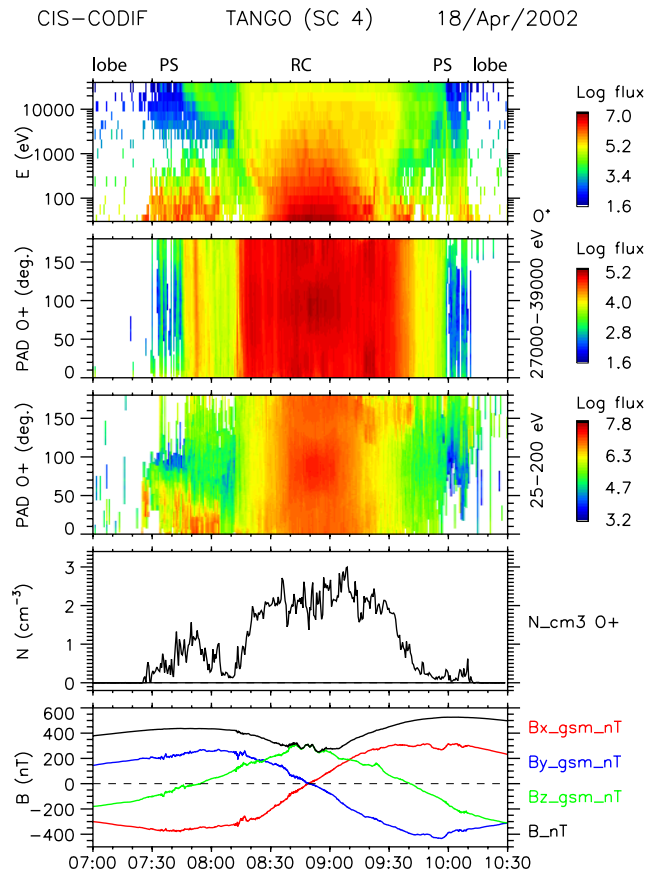

XGSE	−3.14	−3.35	−3.29	−2.88	−2.14	−1.17
YGSE	0.84	1.84	2.69	3.24	3.42	3.25
ZGSE	−4.42	−3.04	−1.42	0.35	2.07	3.59
DIST	5.48	4.89	4.48	4.35	4.54	4.99

Figure 5. Same as Figure 4 but for the oxygen ions.

At 0941 UT, Cluster reentered in the plasma sheet (Northern Hemisphere), also at L $\sim$ 5. Nevertheless, the ring current/plasma sheet boundary was not as sharp as during the inbound pass.

[21] In the oxygen population (see Figure 5), the transition between the lobes and the PS region at 0724 UT is characterized by the detection of upwelling ions, at low energies, and by a trapped high-energy population, as also seen for the protons. Note also that these upwelling low-energy oxygen ions are observed not only in the plasma sheet but also within the ring current region (as deduced by the high-energy particles) but close to its boundaries (e.g., between 0812 and 0818 UT and between 0926 and 0941 UT). The passage inside the RC region is energy dispersed, first seen at higher energies (with a pitch angle distribution showing a field-aligned population as well as a perpendicular one) and then at lower ones (trapped population). The dispersion is more extended for the O^+ population than for the H^+ one. This boundary appears anyway clearly on the oxygen pitch angle distribution, for the 27–39 keV energy range (see Figure 5). Note that the ring current exit, for this event, corresponds to smoother particle flux gradients and is characterized by the coexistence of two types of populations: isotropic high-energy ions, forming the ring current, and low-energy upwelling ions, usually observed at higher magnetic latitudes. The latitudinal extent of the ring current is from ILAT = $-62°$ to ILAT = 64°.

[22] Figures 6a–6c show the HENA hydrogen images and the corresponding inversions at three different times: 0825 UT, 0856 UT, and 0927 UT, for the 27 to 39 keV energy range. This ENA energy channel corresponds to the upper energy range of CODIF. The ENA images in the left panel are taken when the spacecraft was located on the nightside at midlatitudes. The Earth is shown as the circle and dipole field-line pairs are shown for L = 4 and 8 for midnight, dusk, noon, and dawn. The dayside portion of the image is blanked out by the mechanical Sun shutter on the HENA imager. To protect the detector plane from direct sunlight, the shutter closes once every spin when the Sun comes into the FOV of the HENA imager. With the particular orbit configuration of IMAGE, this means that when the apogee is at low latitudes on the nightside, parts of the ring current will be blanked out by the Sun shutter. For this event, the nightside is unaffected by the shutter.

3.3. Analysis

[23] The right panels in Figures 6a–6c show the image inversion results. The resulting proton distributions are plotted in an L-MLT system and black, red, and gray track is plotted annotating the Cluster spacecraft track, projected on this system. The black represents when Cluster was in the inbound plasmasheet, the red represents when it entered the bulk of the ring current, and gray represents the outbound plasmasheet, as identified in the CIS data. The larger red dots in each plot indicate the instantaneous Cluster position (in L-MLT coordinates). The gray contours represent the relative error contours in the inversion. The inner contour represents the 25% relative error and the outer represents the 75% relative error. According to the image inversions, there appears to be a slight increase and broadening of the ring current flux from 0825 UT to 0856 UT and then a slight decrease. Figure 7 shows a time sequence of inversion, from 0754 UT to 0947 UT, of the 27–39 keV hydrogen ENA images. The sequence indicates that there was a gradual increase of proton flux starting at around 0815 UT, peaking at around 0906 UT, followed by a gradual decrease. The increase is consistent with the substorm injection observed at around 0812 UT. The sequence also indicates a slight azimuthal spread of fluxes, but at this time we cannot for certain say if this is due to the drift of the energetic injected plasma westward or if it is due to the change of the region blanked out by the shutter (caused by the slight change in orbital position). We therefore urge the reader not to make any conclusions about the azimuthal spread at this point. Observations of substorm injections and their signatures in ENA images and inversions have been reported by *C:son Brandt et al.* [2002a, 2002b, 2002c]. The decrease between 0906 UT and 0947 UT is most likely caused by out flow from the dayside magnetopause as well as by charge exchange.

[24] As shown, at 0825 UT Cluster is just near the border of the ring current, confirming thus the interpretation made earlier based on the Cluster data, assuming that the four spacecraft were in the ring current, and near its border with the plasma sheet. At 0856 UT, while crossing the equator, Cluster is situated exactly into the bulk of the ring current. The ring current population flux, for protons with energies up to 40 keV, is about 5×10^5 ions/cm^2 sr s keV, according to CIS in situ measurements. Thirty minutes later, the ring current started its decay and Cluster was situated at the border of it again.

[25] We now present a comparison between the proton fluxes, as measured by CODIF on board Cluster SC 4 while crossing the equator, and the ones deduced from the HENA image inversions. This comparison considers the proton population with an energy from 27 to 39 keV, which is the overlapping energy range of the two instruments. Since the HENA image inversions assume an isotropic pitch angle distribution (HENA detects only those ENAs originating from ions whose pitch angle gives an ENA trajectory within the instrument field of view), we cannot compare with 90° particles directly. Owing to the isotropic assumption this comparison cannot be exact. To make a comparison as rigorous as possible, we will only select on CIS data the ion pitch angle range which corresponds to the equatorial pitch angle seen by HENA ($\alpha = 13° \pm 10°$). Also, since the HENA image inversions are given in the equatorial plane, we will only compare the ion flux obtained by HENA image inversion with the one measured by CIS/Cluster while crossing perigee, i.e., the flux recorded at 0856 UT. During this interval, the CODIF background due to penetrating particles from the radiation belts is negligible. Furthermore, HENA is well outside the radiation belts. Averaging the flux over 16 spins (about 1 min data), CIS on spacecraft 4 recorded a flux of about 1.35×10^5 (cm^2 sr s keV)$^{-1}$, whereas the image inversion method gives a flux of about 1.8×10^5 (cm^2 sr s keV)$^{-1}$ for the pixel considered. This implies that the two methods give consistent results within a factor of 1.5.

3.4. Statistical Study

[26] Following the same principles as for the 18 April 2002 event, we present a statistical study for some other events for which Cluster was inside the HENA field of

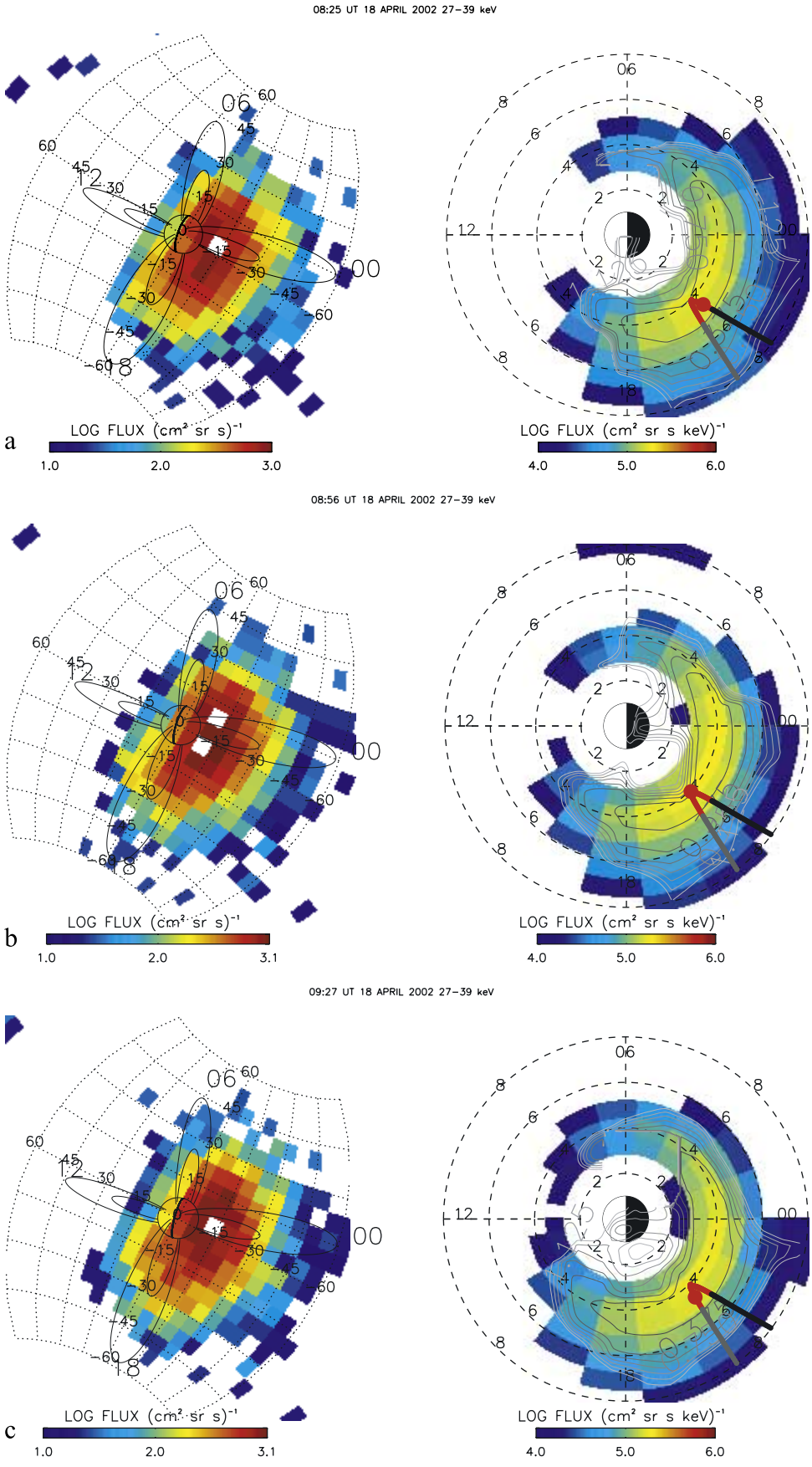
08:25 UT 18 APRIL 2002 27–39 keV
LOG FLUX (cm² sr s)⁻¹
1.0 2.0 3.0
LOG FLUX (cm² sr s keV)⁻¹
4.0 5.0 6.0
a
08:56 UT 18 APRIL 2002 27–39 keV
LOG FLUX (cm² sr s)⁻¹
1.0 2.0 3.1
LOG FLUX (cm² sr s keV)⁻¹
4.0 5.0 6.0
b
09:27 UT 18 APRIL 2002 27–39 keV
LOG FLUX (cm² sr s)⁻¹
1.0 2.0 3.1
LOG FLUX (cm² sr s keV)⁻¹
4.0 5.0 6.0
c

Figure 6

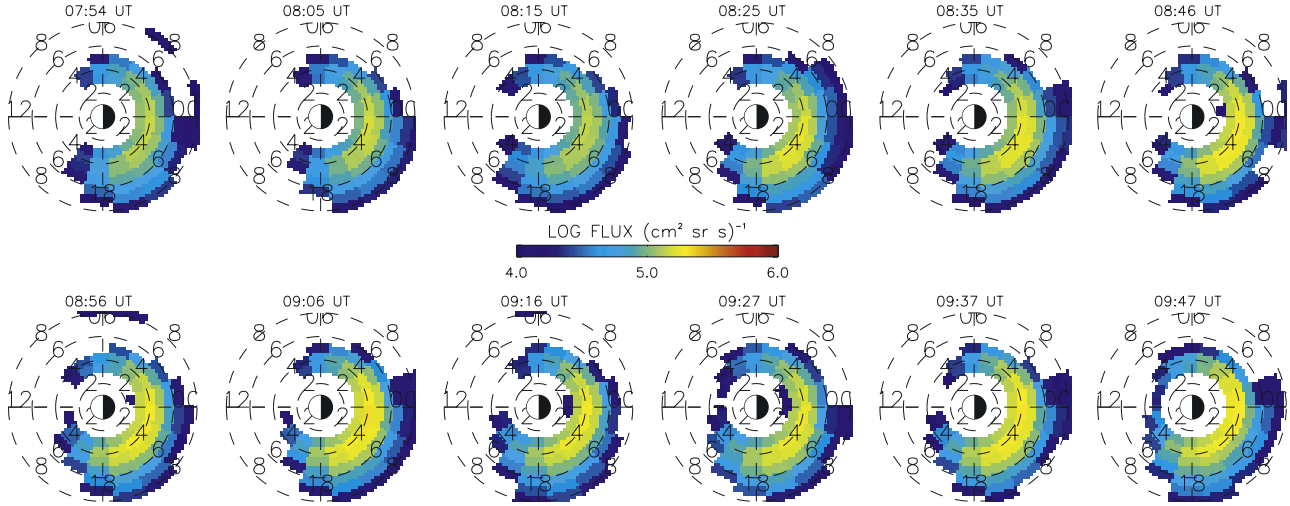

Figure 7. Sequence of inversions from 0754 UT to 0947 UT. Note the gradual increase starting at around 0815 UT and peaking at around 0906 UT, followed by a gradual decrease. This is consistent with the observed substorm injection at around 0812 UT.

view. Events were selected such as to give a range as wide as possible for the magnetic activity levels, as well as for the magnetic local time.

[27] The results of the statistical study are shown in Figure 8 which gives, for each event considered, the proton flux obtained by the HENA image inversion as a function of the in situ proton flux obtained by CODIF on board SC 4 and averaged over 60 s. As for the 18 April 2002 event, the CIS flux, on the equatorial plane, has been limited to the pitch angle values whose population can generate ENAs getting into the HENA field of view, ±10°. We notice that for weak flux values the inversion method seems to systematically over-estimate the ion flux values with respect to the CODIF ones. This is particularly noticeable for the 19 March 2001 event (factor of 32). For higher flux values this tendency is no longer observed.

[28] It thus appears clearly a limitation of the ion flux dynamic range provided by the HENA image inversions; whereas CIS in situ measured fluxes extend over 3 orders of magnitude, HENA's flux range is confined within two orders of magnitude. We should note also the limitation of the statistics due to the small number of good orbit conjunctions between the Cluster perigee passes and the IMAGE apogee passes, as well as the proper operational mode on both instruments.

4. Discussion

[29] During a well-disturbed period (18 April 2002), characterized by a very active ring current, the comparison between the locally measured ion fluxes, by CIS, and the ion fluxes deduced from HENA image inversions reveals a slight overestimation of the second ones but being consistent within a factor of 1.5. This dispersion between the two flux values is often present for the events studied, with a maximum scatter of about one order of magnitude and presenting an in situ measured flux value up to $\sim 10^6$ cm^{-2} sr^{-1} s^{-1} keV^{-1}. In spite of the fact that there are probably instrumental factors that can play a role since the HENA instrument is not a precise instrument but a remote-sensing camera, and since CIS-CODIF can in some cases get background from the radiation belts, there are some other factors which might intervene for the accuracy of the estimation of the ionic fluxes (overestimation or underestimation, depending on the event considered):

[30] 1. The angular resolution: the fluxes deduced from a pixel of the inverted image are an average made over an extended region of the equatorial plan. Note that the angular resolution of the HENA camera (~6°), for the IMAGE apogee (around z = 48,000 km), allows a spatial resolution of about 5000 km when projected onto the equator. Moreover, the bulk of the ring current is quit always confined within ~5 × 5 pixels of the source HENA image. An error made on the source image will thus be extended to a large part of the equatorial plane, when using the inversion method.

[31] 2. Angular scattering: incoming ENAs are scattered when penetrating the front-foil, which produces the start signal for the TOF (time of flight) circuitry. This introduces a point spread of the ENA signal and for the geometric mean of the 27–39 keV channel it is about 12° in the elevation direction (approximately dawn-dusk in the ENA images of Figure 6) and about 9° in the azimuthal direction (approximately noon-midnight in the ENA images of Figure 6). The point-spread function (PSF) is taken into account in the inversion via the response function (see equation (1)).

Figure 6. IMAGE/HENA data for 18 April 2002 and at three different times: (a) 0825, (b) 0856 and (c) 0927 UT. For each time, the figure on the left represents the HENA image of ENAs flux (27–39 keV), and the figure on the right gives the equatorial ion distribution (L-MLT system) as deduced from the HENA image using the inversion method. The red dot represents the Cluster position, as projected on the equatorial plane at these times. The Cluster orbit, projected on this plane, is also shown (see text for details).

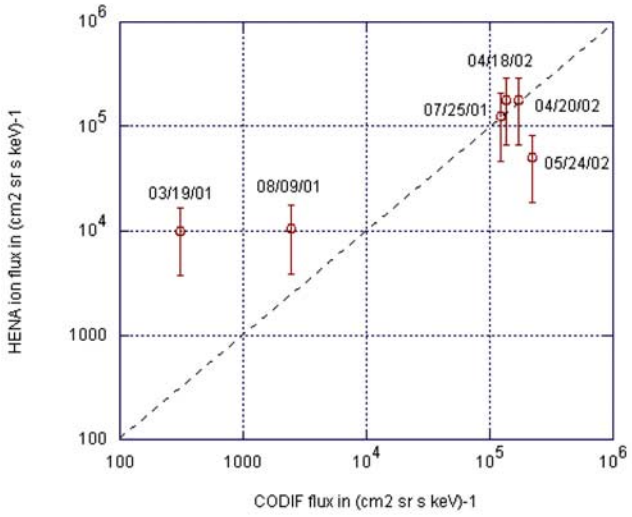

Figure 8. Statistical comparison of the ionic fluxes obtained from the two methods: IMAGE/HENA fluxes (deduced from the ENA image inversions), as a function of in situ measurements made by Cluster/CIS. The dashed line is shown as reference.

[32] 3. From a single vantage point it is impossible to get accurate information on the PAD and we therefore assume isotropic PADs. An ENA detected by HENA represents an ion with a specific pitch angle at the point where the ENA was created. From a vantage point above the North Pole, most ENAs will be produced by ions with pitch angles smaller than 90°. The PADs of the ring current are often more or less peaked around 90° (see Figure 4, panel 2), and it is therefore likely that assuming isotropic PADs in the inversion will underestimate the proton flux. The best one can do is to compare the ion distributions retrieved from the ENA images with proton fluxes away from 90°. Looking at the events for which we made the correlation, it implies that we should expect a better correlation between in situ data and HENA data for events having an isotropic in situ pitch angle distribution. In this study we calculated, for each event, the approximate equatorial pitch angle coming inside the HENA field of view from the Cluster position. We limited the comparison with fluxes (obtained by CIS) measured for a pitch angle distribution centered at ±10° around this specific value.

[33] 4. The inversions in this study assume a dipolar magnetic field model. Tests indicate that this will introduce some smearing and slight shift of the radial location of the resulting ion distribution. Developments are being made to include a stretched magnetic field model. Those tests will be published in a future paper.

[34] 5. The hydrogen exosphere model developed by *Østgaard et al.* [2003] is the most realistic model we have found so far. However, we feel there is still room for improvements, that may affect the retrieved proton fluxes by about 25% in the heart of nightside ring current.

5. Conclusion

[35] Our results show the consistency between the ion fluxes deduced from ENA image inversions and the fluxes measured locally by Cluster. They thus show the complementarity of the two approaches. The locally measured fluxes provide the "ground truth," and they give the detailed ion distributions. ENA images, although restricted by giving access to a portion of the phase space (in terms of pitch angle distributions), allow to position the local measurements with respect to the ring current large scale structure and thus to situate them into a global context.

[36] The measurements made locally in the inner magnetosphere by CIS reveal the existence of very sharp boundaries (about one gyroradius thickness), strongly magnetic field dependent (signature of diamagnetic effects), and the presence of distinct populations, originating from the ionosphere (low-energy upwelling ions observed just outside but also within the ring current), as well as injected from the tail (fresh ring current particles). These latter are also clearly shown in the ENA image inversions.

[37] Our results also point up the limitations of the inversion technique. Images taken from a single vantage point, and which are the source of the inversion technique, are subject to the finite angular resolution of the camera. In addition to that, the inversion technique can introduce other deviations due to the limited precision of the exospheric and magnetic field models used and the line-of-sight integral effect. All these contribute to the uncertainty on the total ion flux estimation, which provokes a substantial scatter of the inversion fluxes with respect to the in situ measured ones, and a more limited dynamic range.

[38] ENA inversions from images taken simultaneously from two (or more) well-separated vantage points, as will be performed with the NUADU (neutral atom detector unit) experiment on board the Double Star spacecraft (S. McKenna-Lawlor et al., An overview of the scientific objectives and technical configuration of the Neutral Atom Dectector Unit NUADU for the Chinese Double Star Mission, submitted to *Planetary and Space Science*, 2004) in association with IMAGE, or with the Two Wide-Angle Imaging Neutral Atom Spectrometers (TWINS) mission, are expected to further reduce these limitations.

[39] **Acknowledgments.** The *Dst* index was provided from the World Data Center for Geomagnetism, Kyoto. We are also grateful to M. Henderson at the Los Alamos National Laboratory for supplying digital SOPA data. This work was in part funded by NASA grant NAG5-12772.

[40] Lou-Chuang Lee thanks Stephen B. Mende and Thomas Earl Moore for their assistance in evaluating this paper.

References

Balogh, A., et al. (2001), The Cluster Magnetic Field Investigation: Overview of in-flight performance and initial results, *Ann. Geophys.*, *19*, 1207.

Burch, J. L. (Ed.) (2000), *The IMAGE Mission*, Kluwer Acad., Norwell, Mass.

Chamberlain, J. W. (1963), Planetary coronae and atmospheric evaporation, *Planet. Space Sci.*, *11*, 901–960.

C:son Brandt, P., R. DeMajistre, E. C. Roelof, D. G. Mitchell, and S. Mende (2002a), IMAGE/HENA: Global ENA imaging of the plasmasheet and ring current during substorms, *J. Geophys. Res.*, *107*(A12), 1454, doi:10.1029/2002JA009307.

C:son Brandt, P., S. Ohtani, D. G. Mitchell, E. C. Roelof, and R. DeMajistre (2002b), Global ENA observations of the storm mainphase ring current: Implications for skewed electric fields in the inner magnetosphere, *Geophys. Res. Lett.*, *29*(20), 1954, doi:10.1029/2002GL015160.

C:son Brandt, P., S. Ohtani, D. G. Mitchell, R. DeMajistre, and E. C. Roelof (2002c), Global ENA observations of a global substorm growthphase dropout in the nightside magnetosphere, *Geophys. Res. Lett.*, *29*(20), 1962, doi:10.1029/2002GL015057.

Daglis, I. A., R. M. Thorne, W. Baumjohann, and S. Orsini (1999), The terrestrial ring current: Origin, formation and decay, *Rev. Geophys.*, *37*, 407–438.

DeMajistre, R., E. C. Roelof, P. C:son Brandt, and D. G. Mitchell (2004), Retrieval of global magnetospheric ion distributions from high energy neutral atom (ENA) measurements by the IMAGE/HENA instrument, *J. Geophys. Res.*, *109*, doi:10.1029/2003JA010322, in press.

Escoubet, C. P., M. Fehringer, and M. Goldstein (2001), The Cluster mission, *Ann. Geophys.*, *19*, 1197.

Jordanova, V. K., L. M. Kistler, J. U. Kozyra, G. V. Khazanov, and A. F. Nagy (1996), Collisional losses of ring current ions, *J. Geophys. Res.*, *101*, 111–126.

Mende, S. B., et al. (2000), Far ultraviolet imaging from the IMAGE spacecraft, *Space Sci. Rev.*, *91*, 287.

Menke, W. (1989), *Geophysical Data Analysis: Discrete Inverse Theory*, Academic, San Diego, Calif.

Milillo, A., S. Orsini, D. C. Delcourt, A. Mura, S. Massetti, and E. DeAngelis (2003), Empirical model of proton fluxes in the equatorial inner magnetosphere: 2. Properties and applications, *J. Geophys. Res.*, *108*(A5), 1165, doi:10.1029/2002JA009581.

Mitchell, D. G., et al. (2000), High-energy neutral atom (HENA) imager for the IMAGE mission, *Space Sci. Rev.*, *91*, 67–112.

Østgaard, N., S. B. Mende, H. U. Frey, G. R. Gladstone, and H. Lauche (2003), Neutral hydrogen density profiles derived from geocoronal imaging, *J. Geophys. Res.*, *108*(A7), 1300, doi:10.1029/2002JA009749.

Perez, J. D., G. Koslowski, P. C:son Brandt, D. G. Mitchell, J.-M. Jahn, C. J. Pollock, and X. X. Zhang (2001), Initial ion equatorial pitch angle distributions from medium and high energy neutral atom images obtained by IMAGE, *Geophys. Res. Lett.*, *28*(6), 1155–1158.

Rairden, R. L., L. A. Frank, and J. D. Craven (1986), Geocoronal imaging with Dynamics Explorer, *J. Geophys. Res.*, *91*, 13,613.

Rème, H., et al. (2001), First multispacecraft ion measurements in and near the Earth's magnetosphere with the identical Cluster ion spectrometry (CIS) experiment, *Ann. Geophys.*, *19*, 1303.

Rodgers, C. (2000), *Inverse Methods for Atmospheric Sounding*, World Sci., River Edge, N. J.

Roelof, E. C. (1987), Energetic neutral atom image of a storm-time ring current, *Geophys. Res. Lett.*, *14*, 652–655.

Roelof, E. C. (1997), ENA emission from nearly-mirroring magnetospheric ions interacting with the exosphere, *Adv. Space Res.*, *20*(3), 361–366.

Roelof, E. C., and A. J. Skinner (2000), Extraction of ion distributions from magnetospheric ENA & EUV images, *Space Sci. Rev.*, *91*, 437.

Sauvaud, J.-A., et al. (2004), Case studies of the dynamics of ionospheric ions in the Earth's magnetotail, *J. Geophys. Res.*, *109*, A01212, doi:10.1029/2003JA009996.

Singer, S. F. (1957), A new model of magnetic storms and aurorae, *Eos Trans. AGU*, *38*, 175–190.

Twomey, S. (1977), *Introduction to the Mathematics in Remote Sensing and Indirect Measurements*, *Dev. in Geomathematics*, vol. 3, 1st ed., Elsevier Sci., New York.

Williams, D. J., E. C. Roelof, and D. G. Mitchell (1992), Global magnetospheric imaging, *Rev. Geophys.*, *30*, 183.

A. Balogh, Blackett Laboratory, Imperial College, South Kensington Campus, London SW7 2AZ, UK. (a.balogh@imperial.ac.uk)

P. C:son Brandt, R. DeMajistre, D. G. Mitchell, and E. C. Roelof, Applied Physics Laboratory, Johns Hopkins University, 11100 Johns Hopkins Rd., Laurel, MD 20723-6099, USA. (pontus.brandt@jhuapl.edu; bob.demajistre@jhuapl.edu; don.mitchell@jhuapl.edu; edmond.roelof@jhuapl.edu)

I. Dandouras, H. Rème, J.-A. Sauvaud, and C. Vallat, Centre d'Etude Spatiale des Rayonnements, 9 avenue du colonel Roche, BP4346, F-31028 Toulouse Cedex 4, France. (dandouras@cesr.fr; reme@cesr.fr; sauvaud@cesr.fr; vallat@cesr.fr)

M. Dunlop, Space Sciences Division, SSTD, Rutherford Appleton Laboratory, Chilton, Didcot, Oxfordshire OX11 0QX, UK. (m.dunlop@rl.ac.uk)

L. Kistler and C. Mouikis, Space Science Center, University of New Hampshire, Durham, NH 03824, USA. (kistler@atlas.sr.unh.edu; cmouikis@atlas.sr.unh.edu)